Transition Metal Migration Can Facilitate Ionic Diffusion in Defect Garnet Based Intercalation Electrodes

Nicholas H. Bashian,[†] Samantha Abdel-Latif,[†] Mateusz Zuba,[‡] Kent J. Griffith,[¶] Alex M. Ganose,[§] Joseph W. Stiles,[†] Shiliang Zhou,[†] David O. Scanlon,[§,||,⊥,#] Louis F. J. Piper,[‡,@] and Brent C. Melot[*,†]

[†]Department of Chemistry, University of Southern California, Los Angeles, CA 90089, USA

[‡]Department of Physics, Applied Physics and Astronomy, Binghamton University, Binghamton, New York 13902, United States

[¶]Department of Chemistry, University of Cambridge, Lensfield Road, Cambridge CB2 1EW, United Kingdom

[§]Department of Chemistry, University College London, 20 Gordon Street, London WC1H 0AJ, U.K.

[||]Diamond Light Source Ltd., Diamond House, Harwell Science and Innovation Campus, Didcot, Oxfordshire OX11 0DE, U.K.

[⊥]Thomas Young Centre, University College London, Gower Street, London WC1E 6BT, U.K.

[#]The Faraday Institution, Quad One, Harwell Science and Innovation Campus, Didcot, U.K.

[@]Materials Science & Engineering, Binghamton University, Binghamton, New York 13902, United States

E-mail: melot@usc.edu

Abstract

The importance of metal migration during multi-electron redox activity has been characterized, revealing a competing demand to satisfy bonding requirements and local strains in structures upon alkali intercalation. The local structural evolution required to accommodate intercalation in $Y_2(MoO_4)_3$ and $Al_2(MoO_4)_3$ has been contrasted by *operando* characterization methods, including X-ray absorption spectroscopy and diffraction, along with nuclear magnetic resonance measurements. Computational modeling further rationalized behavioral differences. The local structure of $Y_2(MoO_4)_3$ was maintained upon lithiation while the structure of $Al_2(MoO_4)_3$ underwent substantial local atomic rearrangements as the stronger ionic character of the bonds in $Al_2(MoO_4)_3$ allowed Al to mix off its starting octahedral position to accomodate strain during cycling. However, this mixing was prevented in the more covalent $Y_2(MoO_4)_3$ which accommodated strain through rotational motion of polyhedral subunits. Knowing that an increased ionic character can facilitate the diffusion of redox-inactive metals when cycling multi-electron electrodes offers a powerful design principle when identifying next-generation intercalation hosts.
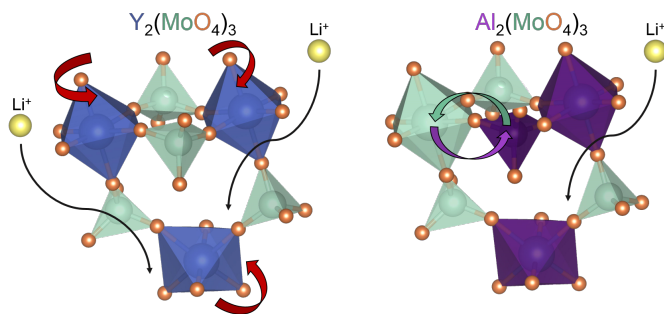
Structural transformations triggered by the transport of alkali ions through the solid state can strongly affect the performance of rechargeable Li-ion batteries.[1,2] Large changes in the unit-cell volume of active materials leads to degradation of electrodes and can eventually fracture the film, creating electrically inaccessible regions within the cell.[3–5] Similarly, substantial atomic rearrangements can complicate Li-ion diffusion pathways and hinder conductivity.[6] Hence, the performance of intercalation battery electrodes is intimately tied to processes that occur at the atomic length scale.[7]

Several charge compensation processes and associated structural changes have been identified which describe a broad range of redox active systems, such as polaron migration and cooperative rotations. The intercalation of Li^+ into V_2O_5 is accompanied by simultaneous polaron migration, leading to local structural distortions and commensurate sluggish ion diffusion.[8] Meanwhile, structural analysis shows that the intercalation of Li^+ into compounds such as ReO_3 is facilitated by cooperative rotations of polyhedral subunits.[9] Furthermore, studies on $Li_{2-x}Ir_{1-y}Sn_yO_3$ show that the substitution of Sn for Ir, and the resulting change in electron count, leads to a different structural change during delithiation, driven by changes in the energies needed to form anti-site defects to stabilize anionic redox behavior.[10] Thus, by considering the electronic structure of materials, it is possible to improve design rules for accommodating alkali intercalation.

To better understand the impact of structural transformations on electrochemical performance, we recently investigated the isostructural phases, $Fe_2(MoO_4)_3$ and $Fe_2(WO_4)_3$, which crystallize in the anti-NASICON structure and consists of corner sharing FeO_6 octahedra joined together by tetrahedrally coordinated Mo or W ions. These materials, originally investigated by Manthiram and Goodenough, exhibit highly reversible cycling on the $Fe^{2+/3+}$ redox couple and can accommodate the insertion of up to two full units of lithium or sodium.[11] We demonstrated that this reversibility is facilitated through the cooperative rotation of the rigid tetrahedral subunits which allows Li^+ or Na^+ ions to move in and out of the structure while minimizing strain within the framework.[12,13] We later built on the work of Greenblatt, Cava, and Murphy to show that similar octahedral rotations occur in the completely unrelated perovskite structure, which appear to be driven by the need to stabilize Li within interstitial cavities that are too large for ions to become fully coordinated.[9,14,15] The nature of the rotations associated with these rigid subunits, which are necessary in densely-packed structures, have wide-ranging impact on multiple facets of electrode performance including Li^+ migration energy barriers, electrode volume change, and reversibility.[16–18]

To broaden our understanding to compounds containing redox active elements in tetrahedral, rather than octahedral, coordination environments, we turned our attention to a pair of molybdates with the general composition $A_2(MoO_4)_3$ where A=Al or Y. While these phases possess homologous compositions to the NASICON family mentioned earlier, they instead crystallize in a defect version of the garnet structure where the cubic site is vacant as illustrated in Figure 1, with octahedral angles provided in S.I. table T2.[19] The inclusion of redox inactive elements on the octahedral site shifts redox activity to occur on the tetrahedral Mo species. Given the record-setting ionic conductivity achievable in stuffed garnets like $Li_7La_3Zr_2O_{12}$ and $Li_6RLa_2Ta_2O_{12}$ (where R=Ca, Sr, or Ba), it would
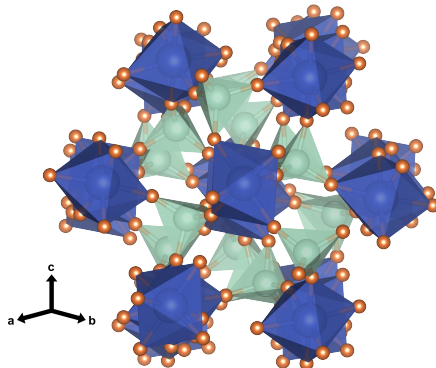
Figure 1: The structure of $A_2(MoO_4)_3$ in space group Pbcn. Molybdenum tetrahedra and redox-inactive octahedra are shown in green and blue, respectively. The AO_6 octahedra create chains, while vacant dodecahedral sites provide space for lithium intercalation.

be highly beneficial to elucidate how incorporating redox-active elements into the framework alters the ability of lithium to move through this unique structural topology.[20–22]

In this letter, we use a combination of *operando* X-ray diffraction and spectroscopic techniques, along with nuclear magnetic resonance measurements and computational modeling to examine how the structural transformations associated with the tetrahedral redox centers in these defect garnets differ from the behavior found for the octahedral sites in the (anti)-NASICON structure. Despite the very similar polyhedral volumes and connectivity, we find a stark contrast in the structural evolution during cycling. In particular, both the Al- and Y-based molybdates exhibit a marked loss of long-range crystallinity after the first cycle, but show a significant difference in local structural evolution We find clear evidence that suggests Mo-ions migrate out of tetrahedral and into octahedral positions in the Al-based material during cycling. We rationalize this metal migration as resulting from the increased ionic character compared to the Y-based analogue, necessitated in order to allow the complete reduction of Mo from the 6+ to the 4+ oxidation state.

$Y_2(MoO_4)_3$ and $Al_2(MoO_4)_3$ were prepared using the techniques described in the Experimental Details section of the Supporting Information. A modified Bellcore method was chosen for electrode preparation during electrochemical testing, which provided compatibility with the *operando* characterization methods employed.[23] Owing to their insulating nature, active materials were combined with a blend of carbon sources to ensure good particle coverage and adequate electrical conductivity. The chosen method of electrochemical testing allowed for ready comparison between *operando* characterization techniques and electrochemistry, creating a more accurate depiction of the behavior of these systems.

The electrochemical properties of $Al_2(MoO_4)_3$ were first evaluated using both cyclic voltammetry and galvanostatic measurements. As seen in Figure 2, the first discharge process consists of a relatively long voltage plateau until three formula units of Li^+ have been inserted, at which point a gradually sloping region begins around 1.85 V. This sloped region persists up to an additional three equivalents of Li^+ until the cutoff of 1.0 V. On reversal, the voltage curve is seen to follow the same solid-solution type profile, yet despite all efforts to optimize the preparation of the
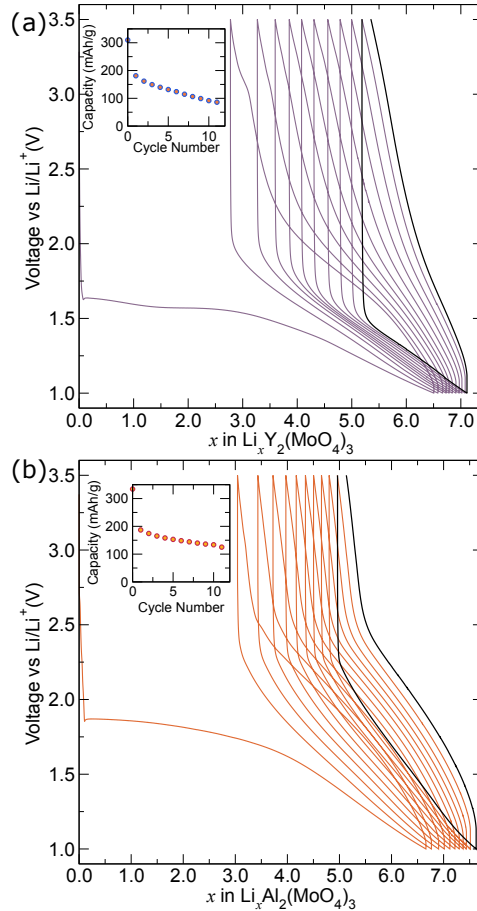
Figure 2: The cycling behavior of (a) $Y_2(MoO_4)_3$ and (b) $Al_2(MoO_4)_3$ shows initial irreversibility followed by smooth cycling. The last cycles in both materials are outlined in black to illustrate polarization differences. The insets demonstrates the capacity fade associated with irreversibility upon cycling.

electrodes it was never possible to remove all six of the intercalated lithium. More typically, a maximum of three lithium could be reversibly cycled between $1.0\,V$ to $3.5\,V$., but as seen in the inset of Figure 2(b) this capacity slowly fades over subsequent cycles. This lost capacity is correlated with a significant loss of diffracted intensity before and after cycling that can be seen in S.I. Figure S1 and will be discussed in greater detail later. Within the garnet crystal structure, the pseudo-octahedral position can accommodate up to six lithium while the empty cubic position can theoretically contain an additional three.[24] Given the size of Li, however, it seems unlikely that it would sit on the cubic site, which more typically contains large ions like those of the alkaline earth metals or lanthanides.[25]

The cyclic voltammogram of $Li_xAl_2(MoO_4)_3$ mirrors the behavior seen in the galvanostatic cycling (S.I. Figure S2) with the initial reductive wave reflecting the irreversibility of the first cycle. The rectangular character of the CV loop suggests a significant capacitive contribution to the charge storage, where both the oxidative and reductive peaks are significantly broadened, extending from $1.0\,V$ to nearly $3.0\,V$, which can be attributed to the solid-solution character of the second insertion process. When taken together, the presence of a single reversible Faradaic feature and the intercalation of six equivalents of lithium per formula unit appears to point towards a reduction of all three Mo ions in the structure from the 6+ to the 4+ oxidation state. Given the insertion of six formula units of Li^+,
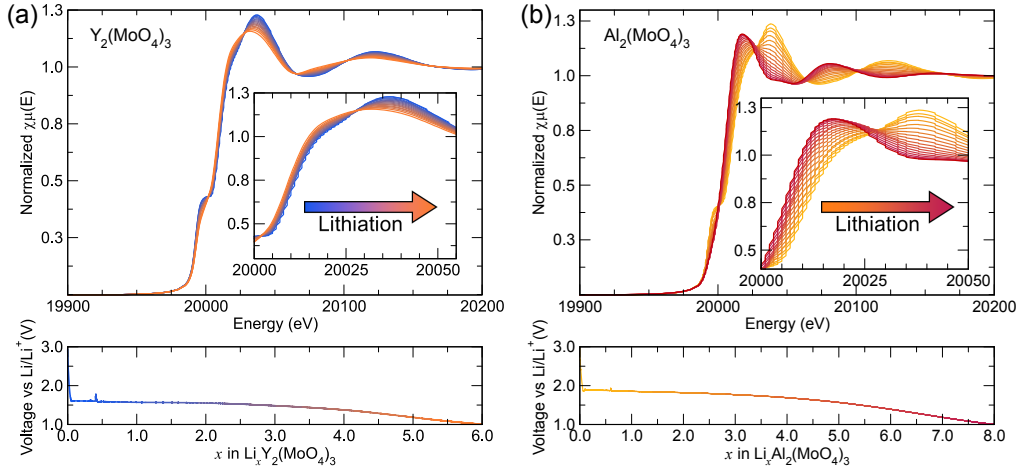
Figure 3: *Operando* XAS measurements were used to track the Mo K-edge in (a) $Li_xY_2(MoO_4)_3$ and (b) $Li_xAl_2(MoO_4)_3$ during lithiation. The XAS spectra are displayed in the top panels, while the corresponding electrochemical data is displayed on the bottom with color change indicating states of lithiation. The electrochemical reduction of Mo^{6+} to Mo^{4+} was correlated to a shift in the Mo K-edge to lower energy. A stronger shift and and restructuring occurred in the Mo K-edge of $Al_2(MoO_4)_3$, indicative of greater change in the Mo local environment, facilitated by metal migration.

along with the associated multi-electron redox, one can expect a large degree of strain to be introduced, necessitating structural change.

Alternatively, Al^{3+} ions may be extruding out of the structure and subsequently plating on the surface of the electrode particles at more reducing potentials, leaving an amorphous form of MoO_3 that continues to cycle.[26] To evaluate this possibility, we turned our attention to the isostructural $Y_2(MoO_4)_3$ which substitutes extremely stable Y ions for the redox promiscuous Al. As seen in Figure 2(a) and S.I. Figure S3, the insertion of Li into $Y_2(MoO_4)_3$ exhibits behavior extremely similar to what was observed for $Al_2(MoO_4)_3$, which suggests the Faradaic reactions most likely involve electronic states derived from the tetrahedral Mo ions. Yet, to remove all doubt, X-ray absorption spectroscopy (XAS) experiments were used to monitor the K-edge of the Y and Mo in a series of *ex-situ* samples at different states of lithiation. As expected, the onset of absorption for Y in $Y_2(MoO_4)_3$ was shifted to lower energy relative to the elemental metal at $17.1\,keV$, consistent with the trivalent oxidation state of the material. More importantly, the X-ray absorption near edge spectroscopy (XANES) region for Y remains essentially constant during lithiation (S.I. Figure S4) reflecting an effectively constant oxidation state for Y while the higher energy EXAFS region clearly shows that the local octahedral coordination environment also remains unchanged (S.I. Figure S5).

In contrast to the Y edge, S.I. Figure S6 shows EXAFS measurements made on the Mo K-edge of the same *ex-situ* samples used for the Y K-edge measurement that indicate the characteristic shift associated with the reduction of Mo as a function of lithiation. The Mo K-edge was subsequently monitored during lithiation using an *operando* technique, which reveals a steady shift from higher to lower energy and evolution of the Mo K-edge in $Y_2(MoO_4)_3$, due to the reduction of Mo^{6+} to Mo^{4+} during lithiation (Figure 3(a)). During this process, a series of isosbestic points are observed, indicative of intermediates formed during the rearrangement of the structure as Li^+ is inserted.

A loss in the pre-edge feature at 20 keV is also seen during lithiation, which is typically only allowed in tetrahedrally coordinated Mo compounds, as it is symmetry forbidden for octahedrally coordinated compounds.[27] Hence, the loss of intensity in this feature represents a distortion of the starting geometry away from ideal tetrahedral geometry as would be expected as the Mo^{6+} is reduced and the bond lengths expand to satisfy local bond valence requirements.

While both the Mo K-edge and pre-edge features change in $Al_2(MoO_4)_3$, there is a far greater restructuring of the Mo K-edge during lithiation of $Al_2(MoO_4)_3$, with a significantly more intense and well-defined peak evolving on reduction, as shown in Figure 3(b). While the isosbestic points observed during the lithiation of $Y_2(MoO_4)_3$ are also present in the Mo K-edge during the lithiation of $Al_2(MoO_4)_3$, we note that the points are somewhat less localized, indicative of greater structural disorder. This suggested a greater degree of structural evolution in the Al-based material that was explored using *operando* X-ray diffraction (XRD) to directly correlate the electrochemical behavior with the evolution of the long-range average structure. Figure 4(a) shows that during the lithiation of $Y_2(MoO_4)_3$, no new peak formation is observed but instead a significant loss of intensity is noted throughout the collection process, indicating a decrease in the crystallinity of the active material. While the absence of any new peaks rules out the formation of any new crystalline phases, it cannot preclude the possibility of amorphous products that would be invisible to average scattering techniques. A loss of long range crystalline order is consistent with the results seen in EXAFS, in which local order is maintained but the order of farther shells is reduced during the discharge process for $Y_2(MoO_4)_3$.

Similar measurements were conducted on the $Al_2(MoO_4)_3$ system, in which the material was seen to lose crystallinity during the lithiation process. It is seen that $Al_2(MoO_4)_3$ decomposes more rapidly, becoming mostly amorphous. Additionally, there is no evidence of new peak formation at higher states of charge, which suggests that crystalline phases are not formed during the lithiation process. These changes are demonstrated in Figure 4(b) which shows the *operando* XRD data collected during the lithiation of $Al_2(MoO_4)_3$. Furthermore, during delithiation there is no evidence of a return to the starting structure, as the peak intensity does not increase during charging, nor do peaks lost during discharge reappear.

Due to the loss of crystallinty during lithiation, the radial distributions from the Fourier transform of the Mo K-edge EXAFS were examined for information about the short-range structural transformations.[28] Despite exhibiting very similar electrochemical behavior, the *operando* EXAFS measurements clearly show that local the coordination environment of the Mo in $Al_2(MoO_4)_3$ and $Y_2(MoO_4)_3$ changes in markedly different ways as demonstrated by the radial distribution plots of the Mo K-edge.

As seen in Figure 4(c), the first coordination shell of $Li_x Y_2(MoO_4)_3$, ranging from 0 Å to 1.6 Å and highlighted with red, maintains a relatively constant intensity at shorter radial distances while longer distances exhibit a loss of definition. Maintenance of the peaks and relative intensity in the red region is indicative of the MoO_4 tetrahedra remaining intact throughout lithiation. In contrast, the second shell, associated with the Mo-Y distances and highlighted in blue, shows the merger of several peaks into a single broad feature; this lost intensity can be attributed
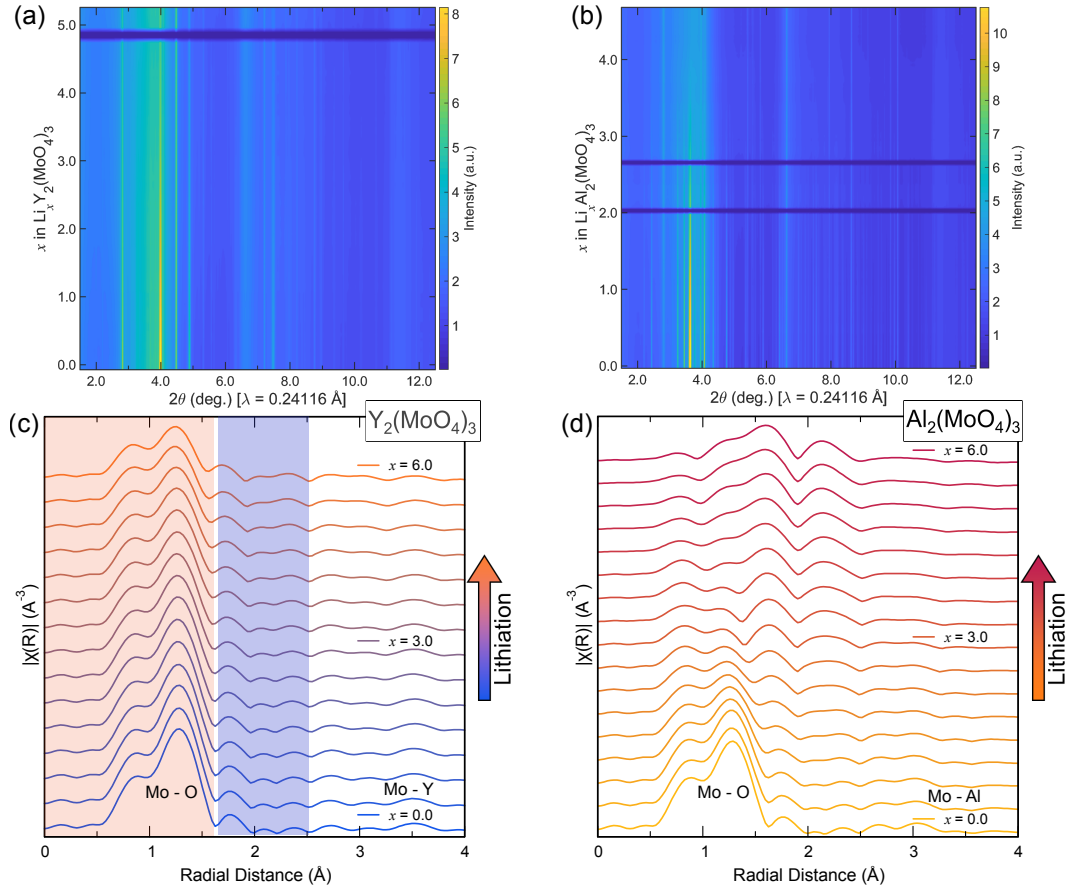
Figure 4: Heatmaps of peak intensities during electrochemical cycling demonstrates the loss of diffracted intensity throughout the cycling process of $Y_2(MoO_4)_3$ (a) and $Al_2(MoO_4)_3$ (b). No new peak formation is observed in either compound, however $Al_2(MoO_4)_3$ is seen to lose peak intensity more rapidly than $Y_2(MoO_4)_3$. The regions of zero intensity (purple) are due to beam outages during data collection. In (c), the radial distribution plot in $Li_xY_2(MoO_4)_3$ obtained from Mo K-edge spectroscopy demonstrating a lack of local structural changes as a function of state of charge. In contrast, in (d), the radial distribution plot in $Li_xAl_2(MoO_4)_3$ exhibits substantial change upon lithiation due to structural rearrangement. The spacing between traces in (c) and (d) represents approximately 0.375 Li^+ inserted with key values and effective scattering distances labeled for clarity.

to a loss of long-range order on lithiation, as tetrahedra undergo short-range rotational disorder and a multitude of scattering paths cancel out. The higher shells exhibit a similar loss of definition in the peaks and significant broadening as the material loses long range order.

Unlike the Y-based phase, the local structure of $Li_xAl_2(MoO_4)_3$ undergoes far more significant structural distortions as lithium is incorporated. In particular, the first shell of the radial distribution function appears to change completely with a significant shift of the peaks to higher scattering lengths, as seen in Figure 4(d). This suggests the tetrahedral Mo coordination environment is lost as lithiation proceeds for the Al-based phase while the evolution of peaks at longer paths appears to suggest a new Mo environment begins to form.

In order to better understand this contrasting behaviors, fits to the radial distribution functions were performed on EXAFS data for the pristine and fully lithiated endpoints of both $Al_2(MoO_4)_3$ and $Y_2(MoO_4)_3$. Fits to the pristine end-members agreed well with the ideal defect garnet starting structure, as shown in S.I. Figures S7(a)

and S7(c) respectively. While the lithiated $Y_2(MoO_4)_3$, in S.I. Figure S7(b) shows very few changes, it is clear from Figure S7(d) that the lithiated form of $Al_2(MoO_4)_3$ undergoes a significant distortion that, after analyzing the fits, appears to represent a transition from tetrahedral MoO_4 to sites more characteristic of octahedral coordination environments, which necessitates a more exaggerated elongation of the Mo–O bonds.

Indeed, by adding an octahedral Mo environment, as could be created if Al and Mo were to switch sites within the structure, it was possible to fit the main peaks of the fully lithiated $Li_6Al_2(MoO_4)_3$ material, as shown in Figure S7(d). As no new crystalline phases are seen in the *operando* XRD, this new site may correspond to a highly disordered derivative of the parent phase where the Mo has migrated out of the tetrahedra and into an environment like the "stuffed" position found in the lithium rich garnet solid electrolytes like $Li_7La_3Zr_2O_{12}$.[29] As this octahedral site is positioned directly between two faces of neighboring tetrahedra, diffusion of Mo-ions could be achieved with minimal structural rearrangement The possibility of Mo-ion diffusion is also consistent with the relatively small polarization seen during the galvanostatic cycling data, which is not typically characteristic of a conversion mechanism into an amorphous product. Additionally, the migration of Mo-ions and associated local structural change is responsible for the larger restructuring observed in the XANES region and the larger spread of isosbestic point in the Mo K-edge during the lithiation of $Al_2(MoO_4)_3$.

While examination of the Al K-edge would be highly beneficial for discriminating between conversion reactions and Mo-ion diffusion, the low X-ray absorption energy of 1.56 keV precludes the collection of useful EXAFS data. Instead, the local coordination of Al was studied using solid-state NMR spectroscopy, which is shown in Figure 5. It can be seen that $Al_2(MoO_4)_3$ exhibits several overlapping resonances between –9 and –14 ppm that agree well with previous measurements (S.I. Figure S8).[30,31] DFT-based calculations on the Al-based material predict a shift range of 4 ppm and nuclear quadrupolar coupling constants (C_Q) of 1.2 ± 0.6 MHz, in agreement with the observed spectrum. Additionally, a broad resonance at 16.0 ppm was seen, which previous ^{27}Al NMR investigations of $Al_2(MoO_4)_3$ by Kunath-Fandrei *et al.* also observed.[30,32] We attribute this signal to a six–coordinate AlO_6 environment, possibly formed by defects in $Al_2(MoO_4)_3$ in which Al occupies the "stuffed" octahedral position between adjacent Mo tetrahedra. Crucially, this peak, along with the other structural peaks are seen to modulate during cycling.

As lithium is inserted into the structure, the ^{27}Al NMR signal for $Al_2(MoO_4)_3$, seen in Figure 5, irreversibly broadens. The negatively shifted resonance almost disappears as lithiation increases to $Li_3Al_2(MoO_4)_3$; it is replaced by a resonance centered at 14.8 ppm. This new resonance may indicate Al movement within the structure, possibly to the "stuffed" octahedral garnet site. This is consistent with the probable octahedral defect at 16.0 ppm in the pristine structure. We note the smaller ionic radii of Al^{3+} in comparison to that of Y^{3+} would allow for more facile ionic migration. The original signal from $Al_2(MoO_4)_3$ is completely absent at the nominal compositions of $Li_5Al_2(MoO_4)_3$ and $Li_{6.5}Al_2(MoO_4)_3$ and a broad new resonance appears around 70 ppm. The ^{27}Al shift of this signal is consistent with four–coordinate aluminum. Furthermore, the shift (75 ± 5 ppm) and C_Q (6 ± 1 MHz) are entirely consistent with aluminum in the four–coordinate garnet site (S.I. Figure S9).[33] The large quadrupolar
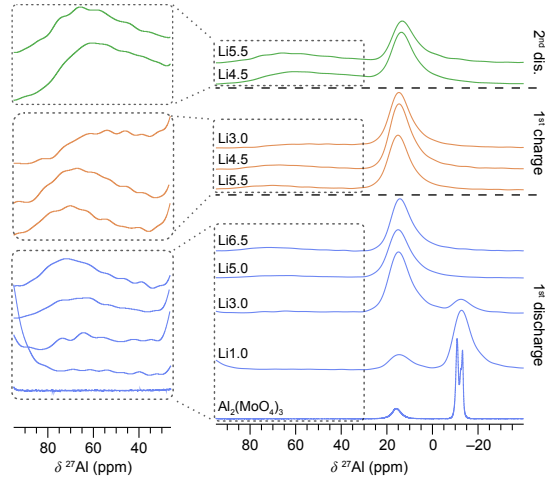
Figure 5: ^{27}Al NMR spectra of Li$_x$Al$_2$(MoO$_4$)$_3$ during the first discharge/charge cycles show the resonances from Al$_2$(MoO$_4$)$_3$ between -9 and -14 ppm; the initial defects assigned to AlO$_6$ and the Li$_x$Al$_2$(MoO$_4$)$_3$ signal that forms on discharge and is assigned to octahedral Al moving to the "stuffed" position at 16 ppm; a second Al environment from Li$_x$Al$_2$(MoO$_4$)$_3$ that is assigned to a four–coordinate site in the garnet at ca. 70 ppm. Expanded views of the region from 30 to 90 ppm are provided in the insets to the left.

coupling constant of this environment indicates highly distorted aluminum coordination, which is consistent with the diffraction showing an increase in local structural disorder on lithium insertion.

If a conversion reaction were occurring, the most likely product would involve the deposition of Al nanoparticles. Al metal resonates at 1640 ppm, giving rise to a sharp signal under MAS; examination of this region in Li$_x$Al$_2$(MoO$_4$)$_3$ showed only spinning sideband intensity from the satellite transitions of the new lithiated phase but no new signals corresponding to the formation of Al metal are visible in S.I. Figure S9 and S.I. Figure S10.[34,35] Furthermore, the normalized ^{27}Al NMR signal in both the fully discharged and charged material is essentially constant, indicating that
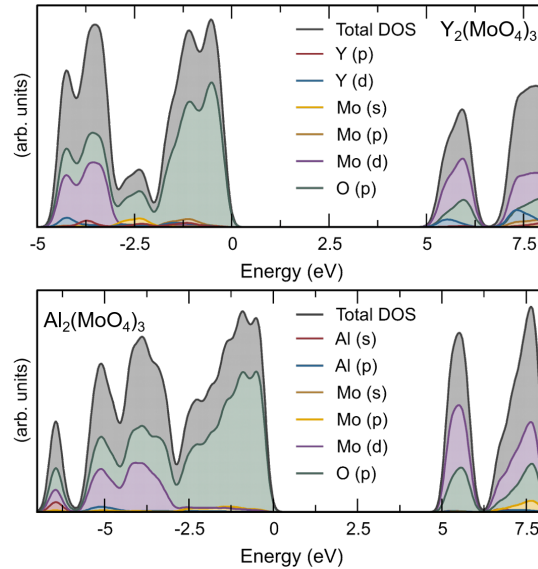

Figure 6: Computed density of states for both Y$_2$(MoO$_4$)$_3$ and Al$_2$(MoO$_4$)$_3$. Note the introduction of Yd-Op states at the bottom of the conduction band.

Al is not removed from the structure. On charging, little change is observed for $Li_{5.5}Al_2(MoO_4)_3$ or $Li_{4.5}Al_2(MoO_4)_3$. At the top of charge, upon removal of 3.5 Li to $Li_3Al_2(MoO_4)_3$, the broad peak at ca. 70 ppm shifts toward lower frequency while the signal at 14.8 ppm is unchanged, as seen in Figure 5. The negatively shifted ^{27}Al resonances of pristine $Al_2(MoO_4)_3$ do not reappear after charging, indicating the irreversibility of the structural transformation. No apparent changes occur on the second discharge. From this evolution of the ^{27}Al NMR spectra, it is clear that the aluminum local environment is irreversibly altered from the $Al_2(MoO_4)_3$ host during the charging process, though no conversion to Al metal nanoparticles is observed. In parallel, the insertion of Li-ions was followed with ^7Li NMR, shown in S.I. Figure S11, but the broad signal centered at −1 ppm neither changed position nor lineshape from initial lithiation through full discharge, charge, or second discharge. ^{89}Y and ^{95}Mo spectra of the host structures are also shown in S.I. Figures S12 and S13.

In order to evaluate the character of the bonding in the two phases and look for a potential origin for difference in the local structural changes, Hybrid Density Functional Theory (DFT) was employed. Both the density of states (DOS) and band dispersions were calculated, as shown in Figure 6 and S.I. Figure S15 respectively. The DOS for both materials exhibits large band gaps on the order of 5 eV with the top of the valence band dominated by Op states while the bottom of the conduction band for both phases contain unoccupied hybrid Mod-Op states. The most significant difference between the two materials is the presence of Yd-Op states at the bottom of the conduction band, which result from the greater orbital overlap between the larger Y^{3+} ions and their oxygen ligands. This increased covalent character of the Y-based phase likely explains the retention of the local structure during cycling given the Y-ions would be far less mobile due to the strong bonds. This can be contrasted against the more ionic character of the bonds in $Al_2(MoO_4)_3$, which allows Al to rearrange during cycling.

Taking these results as a whole, the defect garnet structure exhibits a remarkable ability to incorporate six equivalents of Li per formula, which corresponds to the complete reduction of Mo^{6+} to Mo^{4+} and two electrons per transition metal. Unfortunately, it appears that the number of Li that can be reversibly (de)inserted is restricted

Scheme 1: Differences in bonding between $Y_2(MoO_4)_3$ (a) and $Al_2(MoO_4)_3$ (b) lead to alternate structural distortions upon ion intercalation.
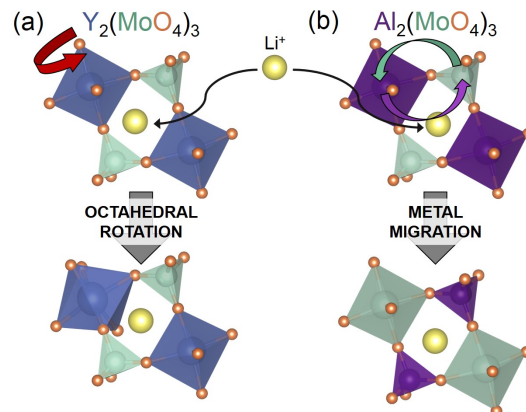
to three, or one per Mo site, which may be related to the significant loss of crystallinity during the initial intercalation. Despite this loss of long-range order, the *operando* EXAFS measurements clearly show the increased covalent character of the Y-based phase preserves the local coordination environment of the polyhedral subunits. In contrast, the predominantly ionic character of the octahedral sites in $Al_2(MoO_4)_3$ results in a redistribution of Al within the structure during the first cycle, which appears to decrease the polarization of the voltage profiles during (de)insertion of Li. We note the similarities with the metal migration proposed by Radin *et al.* as a charge compensation mechanism during the delithiation of lithium-rich manganese oxides, wherein manganese migrates between tetrahedral and octahedral sites.[36] The intercalation of multiple alkali units, along with changing oxidation states necessitates structural changes to accommodate strain, however electronic structure differences lead to multiple possible behaviors. The different mechanisms observed in the $A_2(MoO_4)_3$ ($A=$ Y,Mo) system are further illustrated in Scheme 1, which demonstrates the difference in structural change upon Li^+ insertion.

In summary, the defect garnet polymorph of the $A_2(MoO_4)_3$ family has been studied as a platform for understanding the structural distortions that occur during the two electron reduction of tetrahedrally coordinated Mo^{6+} ions. We have found that the increased ionic character of Al on the A site allows Mo to migrate out of its tetrahedral site and mix into the otherwise vacant "stuffed" octahedral position. This is most likely driven by the difficulty associated with distorting the tetrahedral position in the structure in order to accommodate the lower oxidation state of the tetravalent Mo in the fully intercalated end member. It further highlights the importance of using a diverse set of local structural probes to study systems that lose long-range coherence in their periodic structure during cycling as a way to characterize and understand the complex atomic rearrangements that accompany ionic transport.[37] This work provides critical insight into one of the many ways that extended solids transform during the intercalation of alkali ions like lithium and may help point the way towards accessing the full reversible capacity.

Supporting Information   The Supporting Information is available free of charge.

- Experimental details, including Synthetic Methods, Materials Characterization, Solid State NMR, Electrochemical Characterization, and Computation Methodology; additional cyclic voltammetry measurements; additional X-ray diffraction and X-ray absorption spectroscopy results; Radial Distribution Fits of EXAFS data; additional solid state NMR measurements; additional computational modeling results

Author Information   The authors declare no competing financial interest.

References

(1) Lin, F.; Markus, I. M.; Nordlund, D.; Weng, T.-C.; Asta, M. D.; Xin, H. L.; Doeff, M. M. Surface reconstruction and chemical evolution of stoichiometric layered cathode materials for lithium-ion batteries. *Nat. Commun.* **2014**, *5*, 3529.

(2) Julien, C.; Mauger, A.; Zaghib, K.; Groult, H. Comparative Issues of Cathode Materials for Li-Ion Batteries. *Inorganics* **2014**, *2*, 132–154.

(3) Zhou, G.; Wang, D.-W.; Li, F.; Zhang, L.; Li, N.; Wu, Z.-S.; Wen, L.; Lu, G. Q. M.; Cheng, H.-M. Graphene-Wrapped Fe_3O_4 Anode Material with Improved Reversible Capacity and Cyclic Stability for Lithium Ion Batteries. *Chem. Mater.* **2010**, *22*, 5306–5313.

(4) Sun, Y.; Wang, C.; Xue, Y.; Zhang, Q.; Mendes, R. G.; Chen, L.; Zhang, T.; Gemming, T.; Rümmeli, M. H.; Ai, X.; Fu, L. Coral-Inspired Nanoengineering Design for Long-Cycle and Flexible Lithium-Ion Battery Anode. *Appl. Mater. Interfaces* **2016**, *8*, 9185–9193.

(5) Zhao, Y.; Li, X.; Yan, B.; Xiong, D.; Li, D.; Lawes, S.; Sun, X. Recent Developments and Understanding of Novel Mixed Transition-Metal Oxides as Anodes in Lithium Ion Batteries. *Adv. Energy Mater.* **2016**, *6*, 1502175.

(6) Kang, K.; Meng, Y. S.; Bréger, J.; Grey, C. P.; Ceder, G. Electrodes with High Power and High Capacity for Rechargeable Lithium Batteries. *Science* **2006**, *311*, 977–980.

(7) Poizot, P.; Laruelle, S.; Grugeon, S.; Dupont, L.; Tarascon, J.-M. Nano-sized transition-metal oxides as negative-electrode materials for lithium-ion batteries. *Nature* **2000**, *407*, 496–499.

(8) Jesus, L. R. D.; Horrocks, G. A.; Liang, Y.; Parija, A.; Jaye, C.; Wangoh, L.; Wang, J.; Fischer, D. A.; Piper, L. F. J.; Prendergast, D.; Banerjee, S. Mapping polaronic states and lithiation gradients in individual V_2O_5 nanowires. *Nat. Commun.* **2016**, *7*, 12022.

(9) Bashian, N. H.; Zhou, S.; Zuba, M.; Ganose, A. M.; Stiles, J. W.; Ee, A.; Ashby, D. S.; Scanlon, D. O.; Piper, L. F. J.; Dunn, B.; Melot, B. C. Correlated Polyhedral Rotations in the Absence of Polarons during Electrochemical Insertion of Lithium in ReO_3. *ACS Energy Lett.* **2018**, *3*, 2513–2519.

(10) Hong, J. et al. Metal–oxygen decoordination stabilizes anion redox in Li-rich oxides. *Nat. Mater.* **2019**, *18*, 256–265.

(11) Manthiram, A.; Goodenough, J. B. Lithium insertion into $Fe_2(MO_4)_3$ frameworks: Comparison of M = W with M = Mo. *J. Solid State Chem.* **1987**, *71*, 349–360.

(12) Zhou, S.; Barim, G.; Morgan, B. J.; Melot, B. C.; Brutchey, R. L. Influence of Rotational Distortions on Li^+ - and Na^+ -Intercalation in Anti-NASICON $Fe_2(MoO_4)_3$. *Chem. Mater.* **2016**, *28*, 4492–4500.

(13) Barim, G.; Cottingham, P.; Zhou, S.; Melot, B. C.; Brutchey, R. L. Investigating the Mechanism of Reversible Lithium Insertion into Anti-NASICON $Fe_2(WO_4)_3$. *Appl. Mater. Interfaces* **2017**, *9*, 10813–10819.

(14) Cava, R.; Santoro, A.; Murphy, D.; Zahurak, S.; Roth, R. The structures of lithium-inserted metal oxides: $LiReO_3$ and Li_2ReO_3. *J. Solid State Chem.* **1982**, *42*, 251–262.

(15) Murphy, D.; Greenblatt, M.; Cava, R.; Zahurak, S. Topotactic lithium reactions with ReO_3 related shear structures. *Solid State Ionics* **1981**, *5*, 327–329.

(16) Armstrong, A. R.; Kuganathan, N.; Islam, M. S.; Bruce, P. G. Structure and Lithium Transport Pathways in Li_2FeSiO_4 Cathodes for Lithium Batteries. *J. Am. Chem. Soc.* **2011**, *133*, 13031–13035.

(17) Jesus, L. R. D.; Andrews, J. L.; Parija, A.; Banerjee, S. Defining Diffusion Pathways in Intercalation Cathode Materials: Some Lessons from V_2O_5 on Directing Cation Traffic. *ACS Energy Lett.* **2018**, *3*, 915–931.

(18) Fisher, C. A. J.; Prieto, V. M. H.; Islam, M. S. Lithium Battery Materials $LiMPO_4$ (M= Mn, Fe, Co, and Ni): Insights into Defect Association, Transport Mechanisms, and Doping Behavior. *Chem. Mater.* **2008**, *20*, 5907–5915.

(19) Bruce, P. G., Ed. *Solid state electrochemistry*; Cambridge University Press, 1994.

(20) Murugan, R.; Thangadurai, V.; Weppner, W. Fast Lithium Ion Conduction in Garnet-Type $Li_7La_3Zr_2O_12$. *Angew. Chem. Int. Ed.* **2007**, *46*, 7778–7781.

(21) Thangadurai, V.; Weppner, W. $Li_6ALa_2Nb_2O_{12}$ (A=Ca, Sr, Ba): A New Class of Fast Lithium Ion Conductors with Garnet-Like Structure. *J. Am. Ceram. Soc.* **2005**, *88*, 411–418.

(22) Ahmad, M. M.; Al-Jaafari, A. Concentration and mobility of mobile Li^+ ions in $Li_6BaLa_2Ta_2O_{12}$ and $Li_5La_3Ta_2O_{12}$ garnet lithium ion conductors. *J. Mater. Sci.: Mater. Electron.* **2015**, *26*, 8136–8142.

(23) Tarascon, J.-M.; Gozdz, A.; Schmutz, C.; Shokoohi, F.; Warren, P. Performance of Bellcore's plastic rechargeable Li-ion batteries. *Solid State Ionics* **1996**, *86-88*, 49–54.

(24) Morgan, B. J. Lattice-geometry effects in garnet solid electrolytes: a lattice-gas Monte Carlo simulation study. *R. Soc. Open Sci.* **2017**, *4*, 170824.

(25) Geller, S. Crystal chemistry of the garnets. *Z. Kristallogr. Cryst. Mater.* **1987**, *125*, 1–47.

(26) Schulz, B.; Andersen, H. L.; Bahri, O. K. A.; Johannessen, B.; Liu, J.; Primig, S.; Sharma, N. Electrochemical performance and structure of $Al_2W_{3-x}Mo_xO_{12}$. *CrystEngComm* **2018**, *20*, 1352–1360.

(27) Yamamoto, T. Assignment of pre-edge peaks in K-edge x-ray absorption spectra of 3d transition metal compounds: electric dipole or quadrupole? *X-Ray Spectrom.* **2008**, *37*, 572–584.

(28) Ravel, B.; Newville, M. ATHENA, ARTEMIS, HEPHAESTUS: data analysis for X-ray absorption spectroscopy using IFEFFIT. *J. Synchrotron Radiat.* **2005**, *12*, 537–541.

(29) Awaka, J.; Kijima, N.; Hayakawa, H.; Akimoto, J. Synthesis and structure analysis of tetragonal $Li_7La_3Zr_2O_{12}$ with the garnet-related type structure. *J. Solid State Chem.* **2009**, *182*, 2046–2052.

(30) Kunath-Fandrei, G.; Bastow, T.; Jaeger, C.; Smith, M. Quadrupole and chemical shift interactions of ^{27}Al in aluminium molybdate from satellite transition magic angle spinning NMR. *Chem. Phys. Lett.* **1995**, *234*, 431–436.

(31) Haddix, G. W.; Narayana, M.; Tang, S. C.; Wu, Y. Double-rotation NMR, magic angle spinning NMR, and x-ray diffraction study of the structure of aluminum molybdate. *J. Phys. Chem. A* **1993**, *97*, 4624–4627.

(32) Düvel, A.; Romanova, E.; Sharifi, M.; Freude, D.; Wark, M.; Heitjans, P.; Wilkening, M. Mechanically Induced Phase Transformation of γ-Al2O3 into α-Al_2O_3. Access to Structurally Disordered γ-Al_2O_3 with a Controllable Amount of Pentacoordinated Al Sites. *J. Phys. Chem. C* **2011**, *115*, 22770–22780.

(33) Dupree, R.; Lewis, M. H.; Smith, M. E. Structural characterization of ceramic phases with high-resolution ^{27}Al NMR. *J. Appl. Crystallogr.* **1988**, *21*, 109–116.

(34) Andrew, E.; Hinshaw, W.; Tiffen, R. NMR in rapidly rotated metallic aluminium and cadmium. *J. Magn. Reson.* **1974**, *15*, 191–195.

(35) Wiench, J.; Balema, V.; Pecharsky, V.; Pruski, M. Solid-state ^{27}Al NMR investigation of thermal decomposition of LiAlH$_4$. *J. Solid State Chem.* **2004**, *177*, 648–653.

(36) Radin, M. D.; Vinckeviciute, J.; Seshadri, R.; der Ven, A. V. Manganese oxidation as the origin of the anomalous capacity of Mn-containing Li-excess cathode materials. *Nat. Energy* **2019**, *4*, 639–646.

(37) Boebinger, M. G.; Lewis, J. A.; Sandoval, S. E.; McDowell, M. T. Understanding Transformations in Battery Materials Using in Situ and Operando Experiments: Progress and Outlook. *ACS Energy Lett.* **2020**, *5*, 335–345.